IOP Publishing and International Atomic Energy Agency Nuclear Fusion
Nucl. Fusion **51** (2011) 083050 (15pp) doi:10.1088/0029-5515/51/8/083050

A survey of electron Bernstein wave heating and current drive potential for spherical tokamaks

Jakub Urban[1], Joan Decker[2], Yves Peysson[2], Josef Preinhaelter[1], Vladimir Shevchenko[3], Gary Taylor[4], Linda Vahala[5] and George Vahala[6]

[1] Institute of Plasma Physics AS CR, v.v.i., Association EURATOM/IPP.CR, Prague, Czech Republic
[2] CEA, IRFM, F-13108 Saint Paul Lez Durance, France
[3] EURATOM/CCFE Fusion Association, Culham Science Centre, Abingdon, OX14 3DB, UK
[4] Princeton Plasma Physics Laboratory, Princeton, NJ 08543, USA
[5] Frank Batten College of Engineering and Technology, Old Dominion University, Norfolk, VA 23529, USA
[6] College of William & Mary, Williamsburg, VA 23185, USA

E-mail: urban@ipp.cas.cz

Received 4 April 2011, accepted for publication 13 July 2011
Published 8 August 2011
Online at stacks.iop.org/NF/51/083050

Abstract
The electron Bernstein wave (EBW) is typically the only wave in the electron cyclotron (EC) range that can be applied in spherical tokamaks for heating and current drive (H&CD). Spherical tokamaks (STs) operate generally in high-β regimes, in which the usual EC O- and X-modes are cut off. In this case, EBWs seem to be the only option that can provide features similar to the EC waves—controllable localized H&CD that can be used for core plasma heating as well as for accurate plasma stabilization.

The EBW is a quasi-electrostatic wave that can be excited by mode conversion from a suitably launched O- or X-mode; its propagation further inside the plasma is strongly influenced by the plasma parameters. These rather awkward properties make its application somewhat more difficult. In this paper we perform an extensive numerical study of EBW H&CD performance in four typical ST plasmas (NSTX L- and H-mode, MAST Upgrade, NHTX). Coupled ray-tracing (AMR) and Fokker–Planck (LUKE) codes are employed to simulate EBWs of varying frequencies and launch conditions, which are the fundamental EBW parameters that can be chosen and controlled. Our results indicate that an efficient and universal EBW H&CD system is indeed viable. In particular, power can be deposited and current reasonably efficiently driven across the whole plasma radius. Such a system could be controlled by a suitably chosen launching antenna vertical position and would also be sufficiently robust.

(Some figures in this article are in colour only in the electronic version)

1. Introduction

Present research in electron cyclotron (EC) wave heating and current drive (H&CD) for magnetic confinement thermonuclear fusion [1] is focused on conventional aspect ratio tokamaks, and particularly ITER. However, in the 'alternative' spherical tokamak (ST) with aspect ratio $A \equiv R_0/a$ close to unity (R_0 and a being the major and minor radii, respectively) and weaker external toroidal magnetic field, the usual EC transverse O- and X-modes are mostly cut off and cannot be used for H&CD. The role of ST research is nevertheless very important. For their relatively high neutron flux density and economy, STs are being considered as a candidate for a component test facility (ST-CTF) [2, 3] and, for the same reasons, appear in fusion–fission hybrid concepts [4].

The low magnetic field of STs has a major impact on the propagation of EC waves in the plasma. This frequency range is of crucial importance for auxiliary H&CD systems in present and future tokamaks. Typically, in STs, the electron plasma frequency $\omega_{pe} = 2\pi f_{pe} \equiv (n_e e^2/m_e \varepsilon_0)^{1/2}$ is much higher than the EC frequency $\omega_{ce} = 2\pi f_{ce} \equiv eB/m_e$. Here, n_e is the electron density, B is the total magnetic field, e is the electron charge, m_e is the electron mass and ε_0 is the vacuum permittivity. A similar situation often arises in stellarators, which do not have any principal MHD stability density limits. In this so-called overdense regime,

particularly when $\omega_{pe} > n\omega_{ce}$, $n > 3$ in most of the plasma cross-section, the O- and X-modes of EC waves with first, second and third harmonic frequencies ($\omega_{ce} < \omega < 4\omega_{ce}$) are cut off and cannot propagate inside the overdense plasma. Higher harmonic EC waves are not of interest because of their very weak absorption (low optical depth). However, the electron Bernstein wave (EBW) [5]—a quasi-electrostatic kinetic EC mode—can propagate and be strongly absorbed in an overdense plasma.

EC waves are extremely useful because they can be launched far from the plasma (they do not need large plasma-facing antenna structures such as ion–cyclotron or lower-hybrid waves) and feature highly localized and controllable H&CD capabilities. The application of the overdense mode—the EBW—is, however, complicated by its electrostatic nature. First, EBWs must be excited by appropriately launched O- or X-mode via a so-called OXB or XB mode-conversion scheme. This mode conversion takes place in the upper hybrid resonance (UHR) region, where the wave frequency satisfies $\omega = \omega_{UH} \equiv \sqrt{\omega_{pe}^2 + \omega_{ce}^2}$. This typically occurs near the plasma edge. The mode-conversion efficiency depends on the wave and plasma parameters and is thus a potential source of power loss. The excited EBW can subsequently propagate inside the overdense plasma; however, because of its dispersion characteristics, the propagation strongly depends on plasma parameters and the wave vector can change considerably in various ways (unlike O- and X-mode propagation, during which the parallel wave number is mostly conserved).

H&CD by EBWs have already been demonstrated experimentally in magnetic confinement fusion devices, particularly in COMPASS-D [6] and Wendelstein 7-AS [7, 8]. Numerical studies of advanced (steady-state) spherical tokamak operations consider EBWs as one of the vital current drive systems that can stabilize MHD instabilities [9].

In this paper, we pursue an overall study of EBW H&CD on spherical tokamaks by means of numerical ray-tracing and Fokker–Planck simulations. Two coupled codes—AMR (Antenna, Mode-conversion, Ray-tracing) [10, 11] and LUKE [12, 13]—are employed. These codes have proven to be very suitable for EBWs [11, 14]. A large number of cases with different injection parameters is simulated in four different ST conditions: two experimental discharges of the NSTX tokamak [15], an ST-CTF-like MAST Upgrade H-mode scenario [16, 17] and an NHTX scenario [15]. The resulting extensive collection of results is analysed with emphasis on H&CD performance—viability, effectiveness, flexibility, controllability and robustness.

The paper is organized into five sections. After the introduction, the description of EBW physics involved in this study is given. Section 3 describes the context of the numerical simulation—the target plasmas and the EBW parameters. Numerical results—particularly the current drive localization and efficiency, the role of $N_\parallel$, Z_{eff}, the quasilinear effects and the robustness—are presented in section 4. Finally, section 5 discusses the conclusions of our work.

2. EBW description

The EBW has been known for decades [5]. It appears as another EC branch, in addition to the cold plasma O- and X-modes, when solving the kinetic dispersion relation of a plasma in an external magnetic field. It was later applied to magnetic confinement fusion for H&CD while EBW emission was introduced as a diagnostic tool; an overview of EBW experiments is given in [18]. EBW physics can basically be separated into three areas: the mode conversion, the propagation and the wave-plasma power transfer.

2.1. Mode conversion

The EBW mode conversion is a full wave process in which transverse EC modes and the EBW are involved. The mode conversion always requires the slow X-mode to be excited, which can then fully convert into the EBW at the UHR. This study is confined to EBW excitation from the low-field side (LFS) of a tokamak, where two possibilities exist: the XB [19] and the OXB [20, 21] conversion. The XB conversion is characterized by a direct coupling between the fast and the slow X-mode while in the OXB scheme the O-mode is converted to the slow X-mode (in fact, it is converted to the fast branch of the X-mode, which propagates towards higher density and then smoothly converts to the slow branch, which propagates backwards to the UHR). The XB scheme is typically efficient for lower frequencies and requires the density scale length to be specifically adjusted (for details see [19]). The OXB scheme, on the other hand, is more universal in terms of frequencies and density scale lengths as efficient conversion only requires the O-mode to be incident at the optimum angle. In 1D theory, this angle is given by [20, 23]

$$N_{\parallel opt}^2 = (1 + \omega/\omega_{ce})^{-1}, \qquad N_{pol} = 0, \tag{1}$$

where $\boldsymbol{N} \equiv c\boldsymbol{k}/\omega$ is the normalized wave vector, $N_\parallel \equiv \boldsymbol{N} \cdot \boldsymbol{B}/B$ and $N_{pol} \equiv \boldsymbol{N} \cdot (\boldsymbol{B} \times \nabla n_e)/\|\boldsymbol{B} \times \nabla n_e\|$. If the incident angle is not optimum, the O- to X-mode power conversion efficiency of a plane wave decays approximately exponentially as [21, 23]

$$C_{OX} = e^{-\pi k_0 L_n \sqrt{\omega_{ce}/2\omega}\left(2(1+\omega_{ce}/\omega)\left(N_{\parallel opt} - N_\parallel\right)^2 + N_{pol}^2\right)}, \tag{2}$$

where $L_n \equiv n_e/(\mathrm{d}n_e/\mathrm{d}r)$ is the density scale length, and (2) is evaluated at the O-mode cutoff. This formula agrees well with numerical results for $k_0 L_n > 1$ when $N_\parallel$ is almost optimum [22] so that $C_{OX} > 0.9$. When $N_\parallel$ is further from the optimum, larger $k_0 L_n$ is required for good agreement [22]. A 1D formalism has also been developed [24] which solves the mode-conversion problem for almost arbitrary inhomogeneity scale length. In general conditions, the conversion efficiency must be calculated by full-wave codes, either in the cold plasma [25] or the hot plasma [26] approximation. These codes also take into account the incident wave polarization and the parasitic slow to fast X-mode tunnelling, which can decrease the OXB conversion efficiency, especially when the density gradient is very steep and consequently $k_0 L_n$ is small. Numerical and analytical results are in good agreement particularly around the optimum incidence. As a consequence of the exponential efficiency dependence, there always exists an angular window where the mode conversion is sufficiently effective.

Recently, 2D theory and simulations of the OXB conversion have been developed [27–30]. 2D effects are

shown to be important for off-equatorial launch, where the O-mode cutoff and X-mode cutoff surfaces are no longer parallel [29]. In [30], it is shown that the beam curvature should be matched to the plasma surface curvature in order to optimize the conversion efficiency. The effect of the beam size, which obviously determines the beam spectrum, is also studied, showing that larger beams, i.e. narrower k-spectrum, tend to be more efficiently converted [30]. Nonlinear effects can also play a role, for example a parametric decay [31] or higher harmonic wave generation [32]. Another factor typically not considered in the conversion process is density fluctuations. An estimate, based on a probability distribution function and the 1D formula (2), was made and experimentally demonstrated in [7], showing a considerable decrease in the conversion efficiency for large density scale lengths. A detailed treatment of this problem should employ a 2D approach.

In this paper, even though the mode conversion is not treated in detail, it is nonetheless not neglected. We consider the OXB scheme for its universality. However, the results are directly applicable to any mode-conversion scheme as long as EBWs are excited at the same place with similar $N_\parallel$. The OXB scheme was successfully demonstrated in various past and present experiments [18]. Our EBW H&CD simulation starts from an antenna, which emits a Gaussian beam [33] of a given frequency and waist radius w_0, which, in our case, is calculated from the Rayleigh range

$$z_\mathrm{R} \equiv \pi w_0^2/\lambda_0 = k_0 w_0^2/2, \tag{3}$$

where λ_0 and k_0 are the vacuum wavelength and the wavenumber, respectively. At the distance z_R from the waist, the Gaussian beam doubles its spot size (the beam radius becomes $\sqrt{2}w_0$). At a fixed z_R, the beam divergence is similar for all frequencies. Large divergence, i.e. wide beam k-spectrum, would cause poor O–X conversion efficiency.

We now calculate the conversion efficiency of a Gaussian beam. The electric field of a Gaussian beam in the Fourier space is

$$E \propto \exp\left(-\frac{w_0^2}{4}\left(k_x^2 + k_y^2\right)\right), \tag{4}$$

where $k_{x,y}$ are wave vectors perpendicular to the direction of the beam propagation. The corresponding energy density is $\propto |E|^2$. We can evaluate the total power of the O–X converted Gaussian beam using the analytic formula (2) and Parseval's theorem:

$$\frac{P_\mathrm{OX}}{P_0} = \frac{\int_{-\infty}^{\infty}\int_{-\infty}^{\infty} |E|^2\, C_\mathrm{OX}\, \mathrm{d}k_x\, \mathrm{d}k_y}{\int_{-\infty}^{\infty}\int_{-\infty}^{\infty} |E|^2\, \mathrm{d}k_x\, \mathrm{d}k_y}. \tag{5}$$

We assume here that the error introduced by changing the integration limits from $k_x^2 + k_y^2 \leqslant k_0^2$ to $\pm\infty$ is negligible, which is valid for beams with not too large divergence. We now assume that the $\hat{z}$-axis is along the beam propagation direction and that the launch angle is optimum by setting, without any loss of generality, the magnetic field at the O-mode cutoff to be $\boldsymbol{B}/B = (0, \pm\sqrt{1 - N_{\parallel,\mathrm{opt}}^2}, N_{\parallel,\mathrm{opt}})$. That is, the magnetic field is assumed to be homogeneous across the beam spot at the O-mode cutoff. The integral (5) then becomes

$$\frac{P_\mathrm{OX}}{P_0} = \left[\int_{-\infty}^{\infty}\int_{-\infty}^{\infty} |E|^2 \times \mathrm{e}^{-\frac{\pi L_n\sqrt{\omega_\mathrm{ce}}}{k_0\sqrt{2\omega}}(2(1+\omega_\mathrm{ce}/\omega)(k_0 N_{\parallel,\mathrm{opt}} \mp k_y\sqrt{1-N_{\parallel,\mathrm{opt}}^2} - \sqrt{k_0^2 - k_x^2 - k_y^2 N_{\parallel,\mathrm{opt}})^2 + k_x^2})}\, \mathrm{d}k_x\, \mathrm{d}k_y\right] \times \left[\int_{-\infty}^{\infty}\int_{-\infty}^{\infty} |E|^2\, \mathrm{d}k_x\, \mathrm{d}k_y\right]^{-1}. \tag{6}$$

This can be evaluated analytically after Taylor-expanding the exponent in $k_{x,y}$ around 0 to second order, yielding

$$\frac{P_\mathrm{OX}}{P_0} = \left(1 + 3\frac{\kappa}{z_\mathrm{R}} + 2\frac{\kappa^2}{z_\mathrm{R}^2}\right)^{-\frac{1}{2}}, \tag{7}$$

where $\kappa \equiv \pi L_n\sqrt{\omega_\mathrm{ce}/2\omega}$. This is an important result which, in fact, imposes an upper limit to the conversion efficiency of a Gaussian beam. This limit depends on L_n/z_R for a fixed $\omega_\mathrm{ce}/\omega$. (Note that $0.4 < \sqrt{\omega_\mathrm{ce}/2\omega} < 0.7$ for the first two harmonics.) It also tells us how narrow (i.e. how divergent) a beam can be used while keeping the OXB conversion efficient. The beam conversion efficiency is shown graphically for the discussed scenarios in section 3.2. In a similar fashion, we can also evaluate the conversion efficiency of a Gaussian beam for non-optimum central wave vector.

2.2. *Propagation*

The EBW is, apart from the 'cold' O- and X-modes, a solution to the kinetic (hot) dispersion relation of a plasma in an external magnetic field [5]. Numerous analytical and numerical studies of EBW propagation have been performed and EBW propagation is hence quite well explored. The characteristic properties of EBW propagation are the following.

- The polarization is quasi-electrostatic; hence, in most situations, the electrostatic dispersion relation describes EBWs satisfactorily [34–36].
- EBWs can propagate in plasmas if $\omega_\mathrm{ce} < \omega \lesssim \omega_\mathrm{UH}$[7]. As $\omega \sim n\omega_\mathrm{ce}$, $n = 1, 2, \ldots$, it implies $n\omega_\mathrm{ce} < \omega_\mathrm{UH}$. Note again that EC O- and X-modes are mostly cut off under these conditions. There is no upper density cutoff for EBWs.
- The phase velocity is almost perpendicular to the external magnetic field ($k_\perp \gg k_\parallel$); the group velocity is generally different from the phase velocity in both magnitude and direction.
- The wavelength is of the order of the electron gyroradius $\rho_\mathrm{e} \equiv v_{T_\mathrm{e}}/\omega_\mathrm{ce}$ ($v_{T_\mathrm{e}} \equiv \sqrt{T_\mathrm{e}/m_\mathrm{e}}$ is the electron thermal velocity and T_e is the electron temperature in energy units), i.e.
$$k\rho_\mathrm{e} \cong k_\perp\rho_\mathrm{e} \sim 1. \tag{8}$$
- EBW characteristics vary significantly depending on whether it approaches a resonance at the lower harmonic ($\omega > n\omega_\mathrm{ce}$) or at the higher harmonic ($\omega < n\omega_\mathrm{ce}$). In particular, the perpendicular wave vector is much smaller near the resonance if $\omega < n\omega_\mathrm{ce}$, where $k_\perp\rho_\mathrm{e} \ll 1$ and electromagnetic effects are no longer negligible. Yet, as the wave approaches the resonance, the power is usually absorbed before the electrostatic approximation becomes invalid [34].

[7] $\omega < \omega_\mathrm{UH}$ holds for $\omega < 2\omega_\mathrm{ce}$. Higher frequency EBWs can propagate in a rarified plasma up to a certain lower electron density limit.

- The parallel refractive index $N_\parallel$ evolves during the propagation and can be greater than one (unlike O- and X-modes). Depending on the magnetic field topology and the vertical launch position, the wave parallel index can either stay close to its initial value, or oscillate around zero, or increase/decrease steadily. During the actual EBW propagation, the wave parallel index can change the regime. In general, waves close to the midplane tend to have a flat or oscillating $N_\parallel$ [37], while for off-midplane rays $N_\parallel$ increases or decreases steadily at a rate proportional to the distance from the midplane [19]. This property forms the basis for controlling EBWs.

EBW propagation in a tokamak plasma is far from trivial and necessitates a numerical simulation. The ray-tracing technique is well suited for EBW propagation since the WKB validity conditions are well fulfilled due to the short wavelength. We employ the AMR code [10, 11] to simulate the EBW propagation. This code uses a conventional ray-tracing method [38, 39] with an electrostatic kinetic non-relativistic dispersion relation [40]:

$$\mathcal{D} \equiv 1 + \left(\frac{\omega_{\mathrm{pe}}^2}{k^2 v_{\mathrm{Te}}^2}\right)\left(1 + \sum_n \frac{\omega}{\sqrt{2}k_\parallel v_{T_\mathrm{e}}} \mathrm{e}^{-b} I_n\,(b)\, Z\,(\xi_n)\right) = 0, \tag{9}$$

where

$$\xi_n \equiv \frac{\omega + n\omega_{\mathrm{ce}}}{\sqrt{2}\,|k_\parallel|\, v_{T_\mathrm{e}}}, \qquad b \equiv \left(\frac{k_\perp v_{T_\mathrm{e}}}{\omega_{\mathrm{ce}}}\right)^2, \tag{10}$$

Z is the plasma dispersion function [41] and I_n is the modified Bessel function of the first kind. The ray trajectory is then a solution to the Hamiltonian-type equations

$$\begin{aligned} \frac{\mathrm{d}\boldsymbol{r}}{\mathrm{d}t} &= -\frac{\partial \Re\,(\mathcal{D})}{\partial \boldsymbol{k}} \Big/ \frac{\partial \Re\,(\mathcal{D})}{\partial \omega}, \\ \frac{\mathrm{d}\boldsymbol{k}}{\mathrm{d}t} &= \frac{\partial \Re\,(\mathcal{D})}{\partial \boldsymbol{r}} \Big/ \frac{\partial \Re\,(\mathcal{D})}{\partial \omega}. \end{aligned} \tag{11}$$

Equations (11) conserve $\mathcal{D} = 0$ at zeroth order in the parameter $\Im(\mathcal{D})/\Re(\mathcal{D})$, i.e. in a weak damping approximation.

In this study, we neglect the collisional damping, which can, however, be of critical importance, as was previously shown by our modelling and by experiments at NSTX [42, 43]. Collisional damping is extremely sensitive to edge plasma conditions, particularly the temperature (or, more precisely, the collision frequency) in the mode-conversion layer. As these conditions cannot be sufficiently accurately predicted, we completely ignore the effect of collisions.

By using the non-relativistic electrostatic dispersion (9), we neglect relativistic and transverse electric field effects in the wave propagation. These effects were studied in [34, 44], and also in [45], where a fully relativistic electromagnetic ray-tracing code was used. Some differences are seen in the ray propagation and in the polarization. These differences are, however, rather small and would not change the overall picture of our survey. The fully relativistic approach is also computationally very intensive and would require an extensive amount of computation time to simulate all cases presented here.

2.3. Wave absorption

In this section, we describe the theory of the EBW absorption. EBWs can be absorbed by resonant electrons, which satisfy the resonance condition

$$\omega - n\omega_{\mathrm{ce}}/\gamma - k_\parallel v_\parallel = 0, \tag{12}$$

where $\gamma \equiv (1 - v^2/c^2)^{-1/2}$ is the usual relativistic factor. While the absorption mechanism—the EC harmonic damping—is identical to that for O- and X-modes, the polarization of EBWs is different (quasi-electrostatic), and this leads to a strong interaction even for low temperatures at any EC harmonic. In the ray-tracing approach, the wave absorption is assumed to be weak and can thus be handled independently. This requires the anti-Hermitian part of the dielectric tensor to be much smaller than the Hermitian part, or, alternatively, $\Im(\mathcal{D}) \ll \Re(\mathcal{D})$.

The zeroth order solution of the dispersion relation leads, as shown in the previous section, to the ray-tracing equations (11). The first-order solution then leads to the radiative transfer equation [38]

$$\frac{\mathrm{d}P}{\mathrm{d}t} = \vartheta - \alpha P, \tag{13}$$

where

$$\alpha \equiv -\frac{2\Im\,(\mathcal{D})}{|\partial \Re\,(\mathcal{D})\,/\partial\omega|} \tag{14}$$

is the absorption coefficient, ϑ the emissivity and P the ray power. The non-relativistic dispersion function (9) is, however, inappropriate for the damping calculations. For this reason, the ray-tracing code rather employs the weakly relativistic absorption coefficient by Decker and Ram [34], which is very fast and sufficiently accurate. Assuming high incident ray power P_0, the emissivity can be neglected and the solution to equation (13) is

$$P = P_0 \mathrm{e}^{-\int_0^\infty \alpha\,\mathrm{d}t}. \tag{15}$$

Since equation (15) provides a linear damping solution, any modifications to the electron distribution function by the waves are not taken into account. However, quasilinear effects due to the modified distribution function can play an important role in EC H&CD. For this reason, we employ LUKE—a fully relativistic, bounce-averaged, 3D Fokker–Planck solver [12]—which calculates the evolution of the electron distribution function for axisymmetric plasmas in the low-collisionality regime. LUKE particularly accounts for collisions and quasilinear diffusion due to RF waves. The code uses a fully relativistic, parallel momentum conserving collision operator and a fully implicit 3D time evolution scheme for a fast convergence to the time-asymptotic solution. It has been verified that the damping profile calculated by LUKE in the low power limit agrees with linear theory [13].

2.4. Simulation model

Our model antenna emits a Gaussian beam, parametrized by its frequency, beam waist vertical and radial positions Z_A, R_A and waist radius w_0. The beam radius is, in our case, calculated from the Rayleigh range, therefore fixing the

beam divergence and consequently the beam O–X conversion efficiency (putting aside the variable density scale lengths and the ω_{ce}/ω dependence) for all frequencies.

The antenna angles used in the following simulations are optimized for the OXB mode conversion, i.e. determined by the condition (1) for each beam waist position. The average over a single harmonic frequency range ($n\omega_{ce} < \omega < (n+1)\omega_{ce}$) is chosen as the optimum angle for these frequencies rather than the optimum evaluated for a particular frequency. The differences in the resulting ray-tracing initial conditions are negligible and central ray mode-conversion efficiencies do not drop below 90% in most cases. The launch conditions are also checked using AMR's 1D full-wave calculation [25].

The beam is discretized by a bundle of 16 individual rays. We denote the positions of the intersections of the rays with the beam waist by $\boldsymbol{r}_i^0$, $i = 1 \ldots 16$. Using a straight line propagation, the intersection of the central ray with the O-mode cutoff is found. At this point, the Gaussian beam size is calculated and the beam is again discretized by the same, proportionally scaled 16 ray pattern. We denote these ray spot positions $\boldsymbol{r}_i^1$. The intersections of the straight lines, connecting $\boldsymbol{r}_i^0$ and $\boldsymbol{r}_i^1$, with the O-mode cutoff surface are used as the starting points for ray tracing: i.e. we assume straight propagation of the O-mode from the beam waist to the O-mode cutoff surface, but still taking the beam divergence into account. The initial wave vectors for ray tracing are found by solving the electrostatic dispersion relation (9) with respect to $N_\perp$, using

$$N_{\parallel 0} = \boldsymbol{N}_0 \cdot \boldsymbol{B}/B, \tag{16}$$

where $\boldsymbol{N}_0 = (\boldsymbol{r}_i^1 - \boldsymbol{r}_i^0)/\|\boldsymbol{r}_i^1 - \boldsymbol{r}_i^0\|$ is the ray vacuum wave vector and $\boldsymbol{B}$ is evaluated at the O-mode cutoff.

After finding the initial wave vector, the electrostatic ray tracing is started. The principal results are the ray trajectories and wave vector evolutions. When ray tracing is finished, the outputs are passed to LUKE, along with the magnetic equilibrium and plasma profiles. The AMR–LUKE interface has been particularly verified to keep all quantities consistent. Moreover, the interface is user friendly and LUKE can be launched by AMR, and vice versa, by a single option in the configuration file.

Finally, LUKE determines a distribution function f_{ql} that is consistent with the quasilinear wave absorption. In addition to the flux-averaged absorbed power density profile $P_d(\rho)$, the flux-averaged EBW-driven current density profile

$$j_\parallel(\rho) = -e\left\langle \int v_\parallel f_{ql}\, \mathrm{d}p^3 \right\rangle \tag{17}$$

is also calculated. Here, $\langle\cdot\rangle$ denotes flux surface averaging and ρ is a flux surface coordinate based on the poloidal magnetic flux ψ:

$$\rho = \rho_{pol} \equiv \sqrt{\frac{\psi - \psi_{axis}}{\psi_{LCFS} - \psi_{axis}}}, \tag{18}$$

where ψ_{axis} and ψ_{LCFS} are the poloidal magnetic flux at the magnetic axis and at the last closed flux surface (LCFS), respectively.

Table 1. Fundamental parameters of the target ST scenarios: major radius R_0 (m), minor radius a (m), central toroidal magnetic field B_0 (T), central electron density n_{e0} (10^{19} m^{-3}), central temperature T_{e0} (keV), plasma current I_p (MA).

Name	R_0	a	B_0	n_{e0}	T_{e0}	I_p	Origin
NSTX L-mode	1.0	0.52	0.5	2.6	2.9	0.6	shot 123435
NSTX H-mode	1.0	0.5	0.5	3.9	1.4	1.0	shot 130607
MAST Upgrade	0.93	0.41	0.78	3.5	2.4	1.2	TRANSP
NHTX	1.2	0.37	2.0	20.0	5.7	3.5	TRANSP

3. Simulated scenarios of EBW H&CD

3.1. Fundamental target plasma parameters

As already mentioned in the introduction, EBW H&CD is simulated here in four different target spherical tokamak scenarios, whose fundamental parameters are listed in table 1. As can be seen, the chosen scenarios differ in various fundamental parameters. Two of them are typical NSTX L- and H-mode experimental discharges, the other two are TRANSP (a plasma transport code) [46] model scenarios of the planned MAST Upgrade [17] and of NHTX (a potential plasma-facing component test facility).

The midplane radial profiles of the characteristic frequencies for the target scenarios are plotted in figure 1. The simulated frequency ranges are marked by shaded areas, whose areas delimit the EBW propagation regions, i.e. from the UHR at the edge to the cold EC resonance, which is theoretically accessible by $N_\parallel = 0$ waves only. Clearly, the plasma is overdense ($f_{pe} > nf_{ce}$) and the first three EC harmonics are inaccessible for O- and X-modes in NSTX and MAST. In NHTX, the third harmonic is more or less accessible and the corresponding frequency is compatible with present-day gyrotron technology. The first two EC harmonics have been selected for NSTX and MAST, as higher harmonics will probably be overlapping because of the Doppler broadening. The same applies to NHTX, where, however, only the first harmonic is simulated since the second is only marginally overdense and the OXB conversion region occurs in the core plasma rather than at the plasma edge. Moreover, the high second harmonic frequency (~100 GHz) combined with the relatively long density scale length in the conversion regions makes the OXB mode-conversion angular window rather narrow.

3.2. EBW system parameters

As already shown in numerous previous works (see, e.g. [19, 47]), the propagation path and the $N_\parallel$ evolution of EBW rays strongly depends on the vertical launch position. $N_\parallel$ appears in the resonance condition (12) and can thus influence the wave absorption location. Moreover, $N_\parallel$ is an important factor in the EBW current drive. The vertical launch position is therefore a crucial parameter of any EBW launcher, which, in addition to the frequency, can be chosen arbitrarily. The toroidal and poloidal angles must be optimized for the conversion efficiency and we can only select negative or positive initial $N_{\parallel 0}$. These properties and restrictions dictate the EBW launcher parameters to be scanned in our survey: wave frequency, vertical launch position and the sign of $N_{\parallel 0}$.

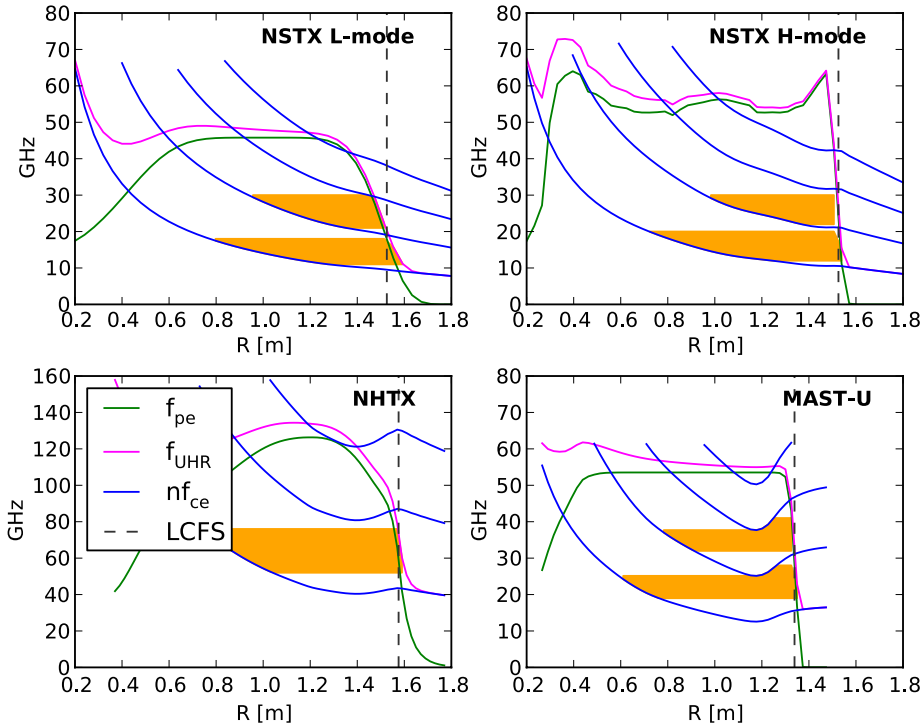

Figure 1. Radial profiles (in the midplane) of the characteristic frequencies for the target scenarios. f_{pe}—electron plasma frequency, f_{UHR}—upper hybrid frequency, nf_{ce}—nth EC harmonic. Filled areas represent the simulated frequency ranges.

Table 2. EBW launcher system parameters used in this study.

Scenario	First harmonic frequencies (GHz)	Second harmonic frequencies (GHz)	Vertical launch positions (m)
NSTX L-mode	11, 11.5, 12, 12.5, 13, 14, 15, 16, 17, 18	21, 22, 23, 24, 25, 26, 27, 28, 29, 30	0, 0.1, 0.2, 0.3, 0.4, 0.5
NSTX H-mode	12, 12.5, 13, 13.5, 14, 14.5, 15, 16, 17, 18, 19, 20	22, 23, 24, 25, 26, 27, 28, 29, 30	0, 0.1, 0.2, 0.3, 0.4, 0.5
MAST-U	19, 20, 21, 22, 23, 24, 25, 26, 28	32, 33, 34, 35, 36, 37, 38, 39, 40, 41	0, 0.1, 0.2, 0.3, 0.4, 0.5, 0.6
NHTX	52, 54, 56, 58, 60, 64, 68, 72, 76	none	0, 0.2, 0.4, 0.6, 0.8, 1.0, 1.2

The waves propagate far enough from the plasma top and bottom so that we can assume up–down symmetry. It has been verified for several cases that the above-midplane launcher power and current density profiles are symmetric with the below-midplane launcher profiles with the opposite sign of $N_{\|0}$. In particular,

$$P(\rho, N_{\|0}, z_A) = P(\rho, -N_{\|0}, -z_A),$$
$$j(\rho, N_{\|0}, z_A) = -j(\rho, -N_{\|0}, -z_A). \quad (19)$$

The reason for this is that the flux surfaces are axially symmetric with respect to the midplane. As a result, EBW rays below and above the midplane are driven in opposite vertical directions with $N_\|$ having opposite signs. Subsequently, the ray paths are symmetric when starting from $\pm z_A$ with opposite $N_\|$, and thus resulting in symmetric power deposition profiles. The opposite sign of $N_\|$ then causes a reversal in the driven current direction.

The frequencies and vertical launch positions used in our survey are given in table 2. The antenna beam Rayleigh range for all simulations is set to 0.5 m. In figures 2 and 3 the maximum Gaussian beam O–X conversion efficiencies calculated from equation (7) for typical target plasma density scale lengths and the dependence on L_n for various Rayleigh ranges are shown. The selected z_R of 0.5 m is a compromise between small beams with poor conversion efficiency and large beams with high conversion efficiency but presumably wide power deposition profiles.

A launcher that would span the whole parameter range listed in table 2 is certainly unrealistic. Multi-frequency systems are rather challenging—even though such systems are actively being studied [48]. For these reasons we focus more on single-frequency systems. A concept of such a system is sketched in figure 4. This system is designed to have a vertically movable mirror, which can be rotated in two dimensions (toroidally and poloidally), thus providing variable vertical launch positions with optimum OXB launch angles at the same time. In-vessel components are shielded from the plasma by screens that can either be part of the machine vacuum vessel (the smaller vessel variant) or placed inside a large MAST-like (cylinder) shape vessel (the larger vessel variant). This system is feasible with present-day technologies and provides enough flexibility required for an advanced EBW system, as will be shown hereinafter.

The principle of using EBW control based on a vertically adjustable launcher is demonstrated in figure 5. It is clearly seen that the vertical launch position (in addition to the frequency) has a major effect on the ray propagation and strongly influences the location of the power deposition. We also notice the typical behaviour of EBW rays: midplane rays with frequencies for which the cold EC resonance surfaces (typically concave shaped) occur in the inboard half of the

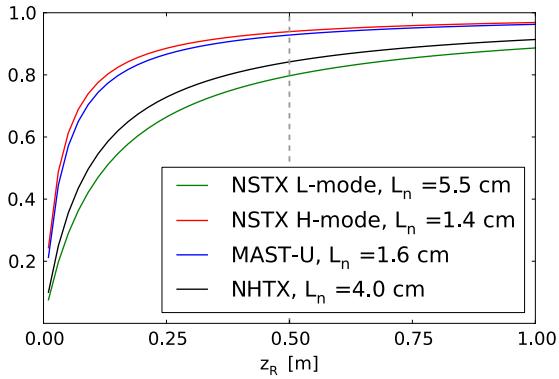

Figure 2. Gaussian beam maximum conversion efficiency, equation (7) dependence on z_R. The average L_n in the mode-conversion region is used; $\omega_{ce}/\omega = 0.5$.

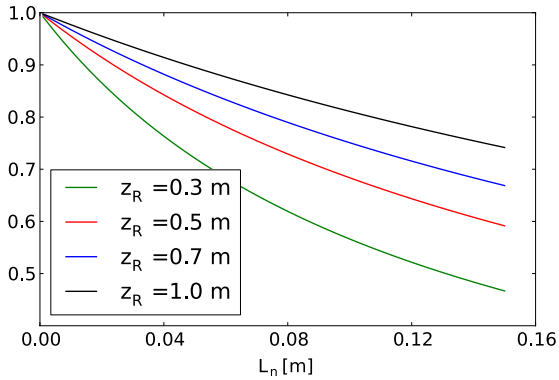

Figure 3. Gaussian beam maximum conversion efficiency, equation (7) dependence on L_n; $\omega_{ce}/\omega = 0.5$.

plasma typically propagate straight until they reach the vicinity of a cold EC resonance, where their $|N_\parallel|$ grows exponentially and the rays are damped [37]. Rays with lower frequencies, whose cold EC resonance layers appear in the outboard half with typically convex shape, oscillate around the midplane and their $N_\parallel$ oscillate around zero [37]. Rays launched off-midplane are characterized by steadily and monotonically varying $N_\parallel$. This behaviour is shown graphically in section 4.2. This results in a significant Doppler shift of the EC frequency and hence these waves are absorbed quite far from the cold resonance.

4. EBW H&CD performance—numerical results

In this section, we present our result on EBW H&CD performance in the previously listed scenarios. The mode conversion, which is a well-separable problem, is always assumed to be 100%. There are two fundamental reasons for this assumption. First, we would like to focus on EBW propagation, absorption and current drive. These aspects, as will be shown hereinafter, are complex enough even when neglecting the mode conversion. Second, the theoretical description of the mode-conversion process is so complex that we can arrive to almost any results depending on which theories and processes are considered. Moreover, the knowledge of the edge plasma, where the mode conversion occurs, is very limited.

4.1. Localization and current drive efficiency

The current drive efficiency can be expressed in various ways. The most straightforward and suitable from the experimental and engineering point of view is the absolute efficiency

$$\eta \equiv \frac{I_{RF}}{P_0}, \tag{20}$$

where I_{RF} is the total current driven by the RF waves and P_0 is the total injected RF power. However, the current drive efficiency unavoidably depends on plasma parameters, particularly the collisionality, and hence a quantity that reflects this intrinsic behaviour would be better suited for comparing different plasmas and current drive mechanisms. Commonly used for EC waves is the normalized efficiency ζ [49], which scales out the electron density and temperature collisional effects and the plasma size. However, ζ does not reflect the intrinsic effects of particle trapping and effective ion charge (Z_{eff}). The original definition assumes that the power deposition profile is well localized so the plasma parameters (density and temperature) do not change there. This is not always valid and we therefore use an absorbed power weighted average:

$$\zeta \equiv \frac{e^3}{\varepsilon_0^2}\frac{R_0}{P_0}\int \frac{n_e(\rho)}{T_e(\rho)}\frac{dI_{RF}}{d\rho}d\rho. \tag{21}$$

Here, dI_{RF} is the RF-driven current in a plasma surface enclosed by ρ and $\rho + d\rho$ flux surfaces. In the numerical simulations, LUKE selects a ρ-grid (based on the power deposition profile) so the volumes become finite:

$$\Upsilon_i \equiv V\left(\frac{\rho_i - \rho_{i-1}}{2}, \frac{\rho_{i+1} - \rho_i}{2}\right), \tag{22}$$

where $V(\rho, \rho')$ denotes the plasma volume enclosed by the flux surfaces ρ and ρ'. ρ_i are the LUKE grid points. The discrete form of (21) is then

$$\begin{aligned}\zeta &= \frac{e^3}{\varepsilon_0^2}\frac{R_0}{P_0}\sum_i \frac{n_e(\rho_i)}{T_e(\rho_i)} I_i \\ &\cong 3.27\frac{R_0\,[\mathrm{m}]}{P_0\,[\mathrm{W}]}\sum_i \frac{n_e(\rho_i)\left[10^{19}\,\mathrm{m}^{-3}\right]}{T_e(\rho_i)\,[\mathrm{keV}]} I_i\,[\mathrm{A}],\end{aligned} \tag{23}$$

where I_i is the current driven in the poloidal cross-section of Υ_i. Note that ζ reflects the sign of the driven current.

In figures 6–9 we show the current drive efficiency ζ for all plasma and launch scenarios listed in table 2, i.e. for the different frequencies, vertical launch positions and toroidal injection directions. The classification of the current drive mechanism is performed automatically by calculating the average (absorbed power weighted) $N_\parallel$ of the rays and subsequently comparing the LUKE-calculated current direction to Ohkawa and Fisch–Boozer current directions. In certain cases, this leads to ambiguous results, either because the rays have mixed signs of $N_\parallel$ or they are absorbed at different harmonics. The results were obtained by AMR and LUKE coupled simulations with 1 MW incident power. We immediately notice the importance of the launch parameters as they strongly influence the location of the wave power deposition (which obviously coincides with the driven current location) and the current drive efficiency in a fixed plasma equilibrium. Clearly, by changing these parameters, we can

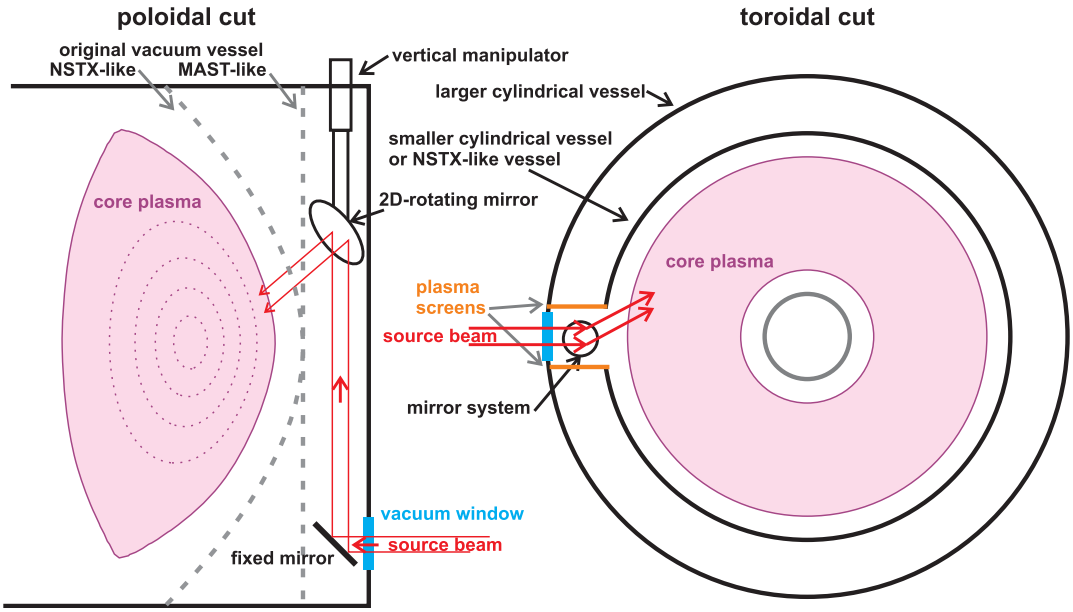

Figure 4. A possible concept of an EBW launcher system with a vertically movable antenna. The design is sketched for two (existing) vacuum vessel shapes—NSTX-like (spherical) and MAST-like (cylindrical). Two variants are proposed—either inside a larger vessel or outside a smaller vessel.

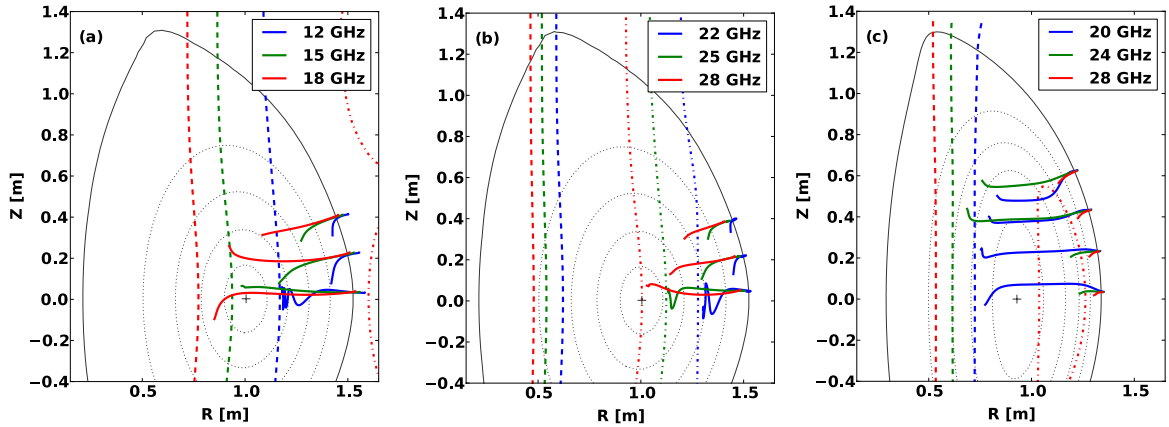

Figure 5. Ray trajectories for various frequencies and vertical launch positions for (*a*) NSTX L-mode, first harmonic, (*b*) NSTX L-mode second harmonic, (*c*) MAST-U first harmonic. Ray trajectories are plotted with solid lines, dashed and dashed–dotted lines show first and second cold EC resonance surfaces, respectively.

select a specific scenario—on/off axis deposition at almost any ρ with high/low $|\zeta|$. There is full flexibility in the direction of the driven current because of the (a)symmetry (19). EBWs are most flexible and efficient in driving current in NSTX plasmas, mainly because in this case the magnetic field is monotonic without any magnetic well in the edge region. $|\zeta| \cong 0.4$ can be reached at almost any radius in NSTX. Our current drive efficiencies are similar to experimental values from COMPASS-D [6] or Wendelstein 7-AS [8] as well as to numerical results obtained for MAST-U [50] or NSTX [51].

While similar efficiencies can be reached using EC X- and O-modes in the central region, the X- and O-mode current drive efficiency typically decreases with radius, particularly because of trapping effects (see, e.g. [49]), which is not the case with EBWs. The L-mode plasma parameters cause higher absolute current drive efficiency, i.e. higher η/ζ. There exist several significantly higher efficiency second harmonic cases with $\rho \cong 0.1$ (i.e. almost on the magnetic axis) in both L- and H-modes. Even though the results reported here indicate a limited on-axis accessibility and flexibility, this may not necessarily hold for slightly different frequencies or launch positions.

Typically we find that in the central plasma regions we drive a Fisch–Boozer current [52] while Ohkawa current [53] in edge regions. Higher harmonic absorption, i.e. absorption on the nth harmonic with $n\omega_{ce} > \omega$, favours the Ohkawa mechanism. Typically we can distinguish three EBW efficient current drive regions:

(i) Fisch–Boozer current drive with lower harmonic absorption predominantly near the centre.
(ii) Ohkawa current drive with lower harmonic absorption predominantly near the edge.
(iii) Ohkawa current drive with higher harmonic absorption predominantly between the plasma centre and edge (i.e. between the first and second regions).

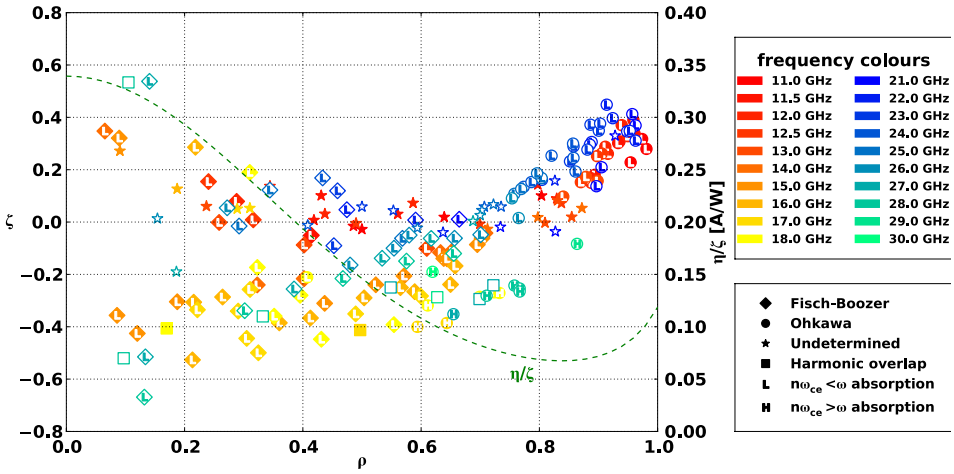

Figure 6. Current drive efficiency ζ (symbols) and η/ζ conversion factor (dashed line) versus ρ, NSTX L-mode first (full symbols) and second (open symbols) harmonics, all frequencies and vertical launch positions as listed in table 2, both positive and negative $N_{\|0}$, 1 MW incident power. Neither the vertical launch position nor the $N_{\|0}$ sign can be graphically distinguished in the figure.

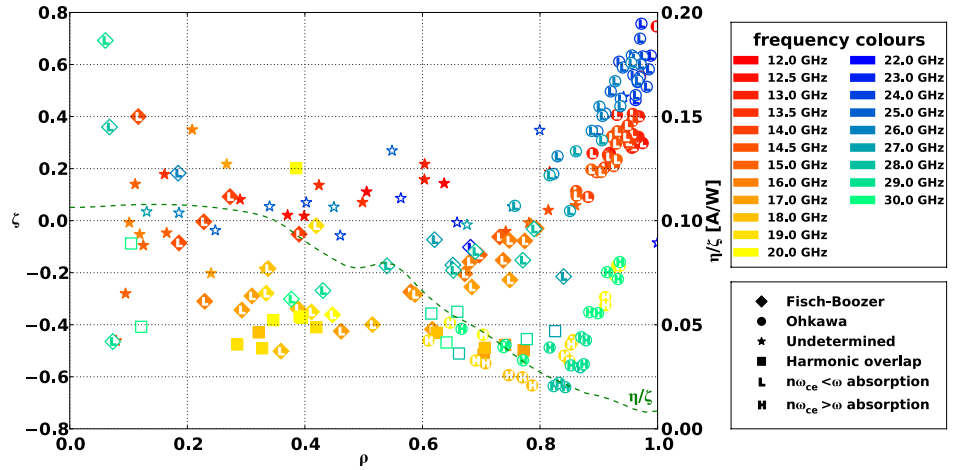

Figure 7. Same as figure 6, but for the NSTX H-mode.

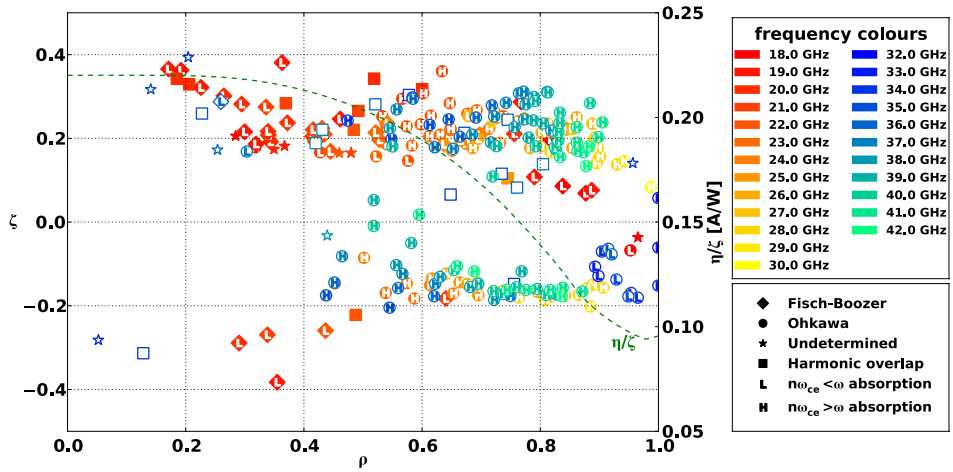

Figure 8. Same as figure 6, but for the MAST-U plasma.

The location and size of these regions are very different in the investigated plasmas and these regions typically overlap. There also exist cases when the harmonics are overlapping, i.e. the wave is absorbed on two different EC harmonics. Quite interestingly, in these cases the current is still driven in one direction even though the resonant electrons have their $v_{\|\mathrm{res}}$ having different signs. This occurs because the lower harmonic absorption favours the Fisch–Boozer mechanism (for which

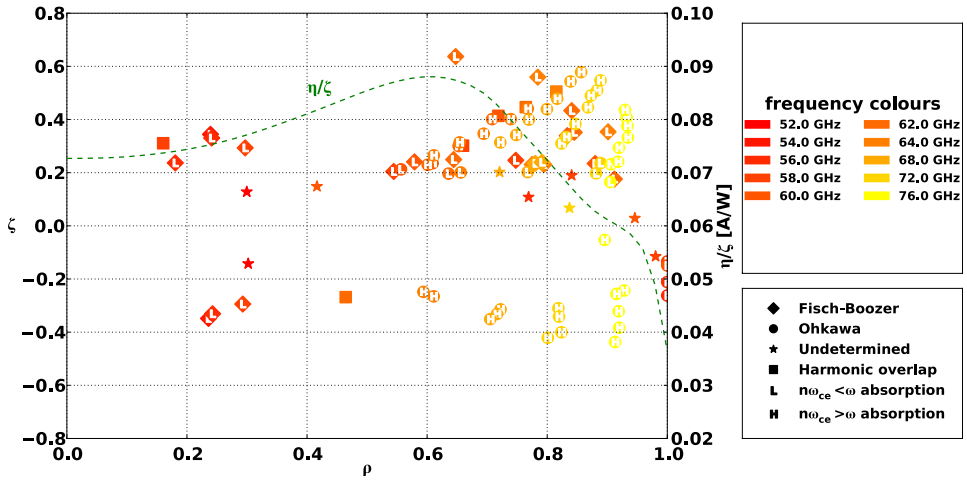

Figure 9. Same as figure 6, but for the NHTX plasma.

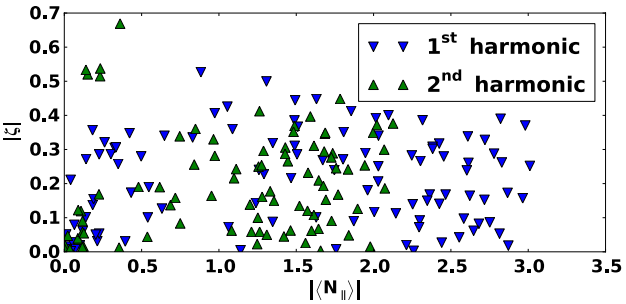

Figure 10. Current drive efficiency versus the magnitude of the mean $N_\parallel$, for all NSTX L-mode cases, $P_0 = 1$ MW.

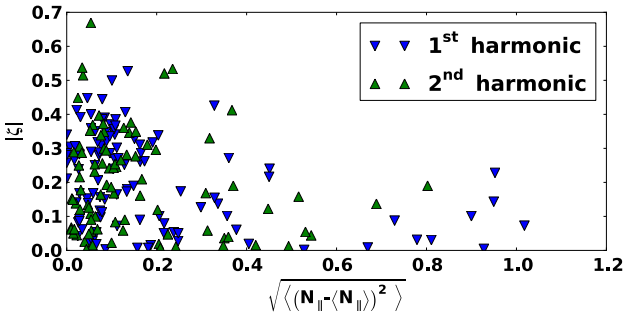

Figure 11. Current drive efficiency versus absolute variance of $N_\parallel$, for all NSTX L-mode cases, $P_0 = 1$ MW.

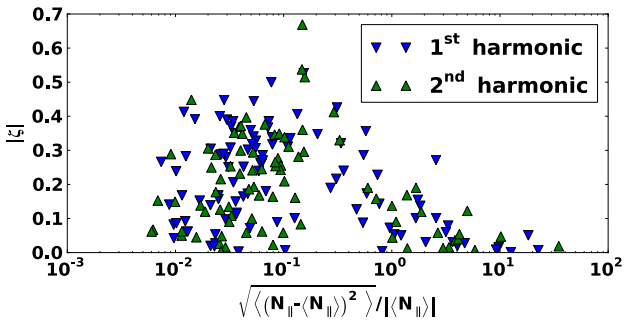

Figure 12. Current drive efficiency versus relative variance of $N_\parallel$, for all NSTX L-mode cases, $P_0 = 1$ MW.

$v_{\parallel \mathrm{res}} \cdot j < 0$), while the higher harmonic absorption favours the Ohkawa mechanism (for which $v_{\parallel \mathrm{res}} \cdot j > 0$).

In going from an NSTX L-mode to an NSTX H-mode to a MAST-U and then to an NHTX plasma, the external magnetic field increases together with the appearance of magnetic wells near the edge (these wells being caused by strong edge currents) and we observe a decrease in the current drive efficiency, as well a decrease in the flexibility of the EBW absorption and central plasma accessibility.

4.2. $N_\parallel$ and quasilinear effects

In order to show the effects of $N_\parallel$, we calculate its average value (not to be confused with the initial $N_\parallel$), weighted by the absorbed power:

$$\langle N_\parallel \rangle = \frac{\sum_i \Delta P\,(\Upsilon_i)\, \frac{\sum_{\text{rays},\ \rho \in \Upsilon_i} N_\parallel \Delta P_{\text{ray}}(N_\parallel, \rho)}{\sum_{\text{rays},\ \rho \in \Upsilon_i} \Delta P_{\text{ray}}(N_\parallel, \rho)}}{\sum_i \Delta P\,(\Upsilon_i)}. \qquad (24)$$

Figure 10 shows the current drive efficiency versus $|\langle N_\parallel \rangle|$. It is found that the two quantities are clearly uncorrelated. As a consequence of the short wavelength of EBWs ($k_\perp \rho_e \sim 1$), the resonant $v_\perp$ is low, irrespective of the value of $N_\parallel$. The dominant factors in EBW CD efficiency are the $N_\parallel$-spectrum (mixing of signs), harmonic overlapping (because of large $|N_\parallel|$) and Fisch–Boozer versus Ohkawa effects.

Figures 11 and 12 show the current drive efficiency versus the absolute and the relative $N_\parallel$ variance: again, we find no clear correlation. There is only a weak (logarithmic) decrease with the relative variance, starting at ∼0.1. Most of the cases have a rather narrow $N_\parallel$ spectrum, with absolute variance <0.2 and relative variance <0.1. NSTX H-mode, MAST-U and NHTX results show very similar behaviour.

We now compare the effect of two different vertical launch positions for the NSTX L-mode plasma at frequency 17 GHz. The ray trajectories and the evolution of $N_\parallel$ are plotted in figure 13. Those rays launched close to the midplane propagate straight to the magnetic axis, and the central ray's $N_\parallel$ does not change appreciably until the ray gets close to the resonance (around $R = 1$ m). $|N_\parallel|$ now starts to increase exponentially,

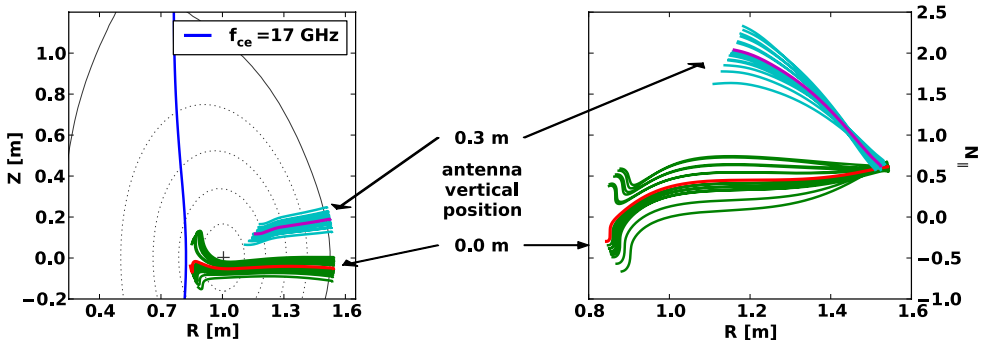

Figure 13. Ray trajectories and the evolution of $N_\parallel$ for two NSTX L-mode cases at 17 GHz with different vertical launch positions: 0 and 0.3 m.

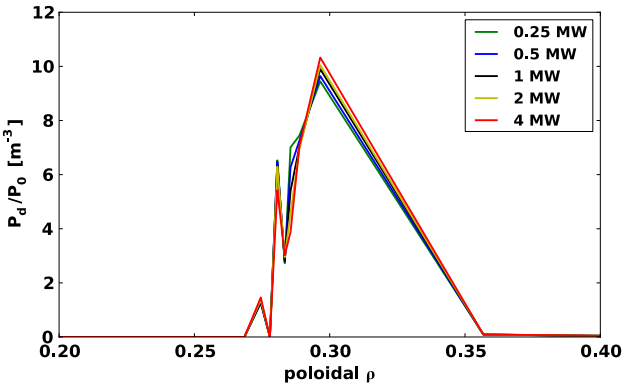

Figure 14. Power deposition radial profile, NSTX L-mode, 17 GHz, 0.0 m vertical launch position.

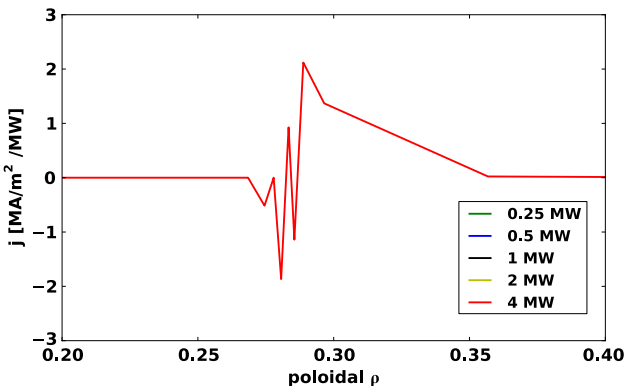

Figure 15. Driven current density radial profile, NSTX L-mode, 17 GHz, 0.0 m vertical launch position.

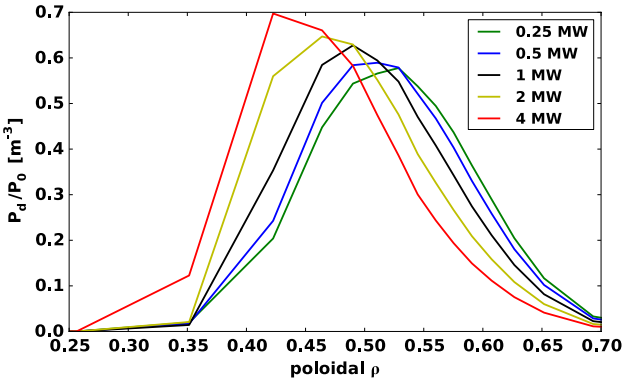

Figure 16. Power deposition radial profile, NSTX L-mode, 17 GHz, 0.3 m vertical launch position.

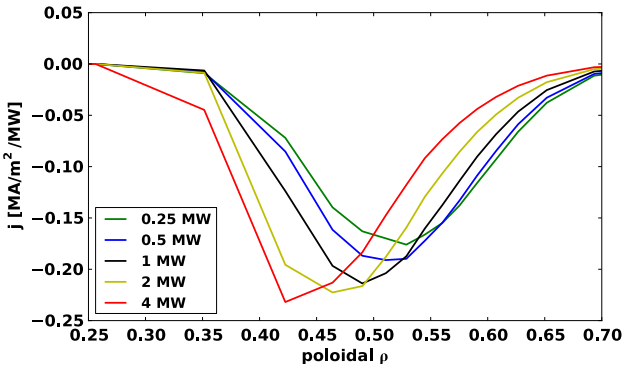

Figure 17. Driven current density radial profile, NSTX L-mode, 17 GHz, 0.3 m vertical launch position.

and the beam splits into two parts that propagate in opposite vertical directions. Finally, the rays are absorbed, having been split in approximately two halves with opposite signs of $N_\parallel$ at the absorption location. This behaviour demonstrates the typical behaviour of midplane rays at frequencies where the cold EC resonance surface is lying in the inboard half of the plasma. For off-midplane launch at 17 GHz, one sees in figure 13 that $|N_\parallel|$ steadily increases and the waves are absorbed at an EC resonance that has been Doppler shifted. Since all rays have the same sign in $N_\parallel$ signs, one achieves a high current drive efficiency.

These two examples clearly demonstrate how the deposition location and the current drive efficiency can be controlled by the choice of the vertical launch position. In figures 14–17 we see the resulting power deposition and driven current densities, plotted for launched powers from 0.25 to 4 MW. The power deposition profile (and consequently the driven current profile) is rather narrow in the midplane launch case (figures 14 and 15), since there is a sharp resonance close to the cold EC resonance surface. The driven current profile is oscillating around zero, resulting in nearly zero net driven current. These oscillations are rather artificial, partly because of the beam discretization by individual rays, and partly because, in reality, such oscillations would most probably be smoothed out by radial transport. There is almost no dependence on the launched power because of the sharp resonance.

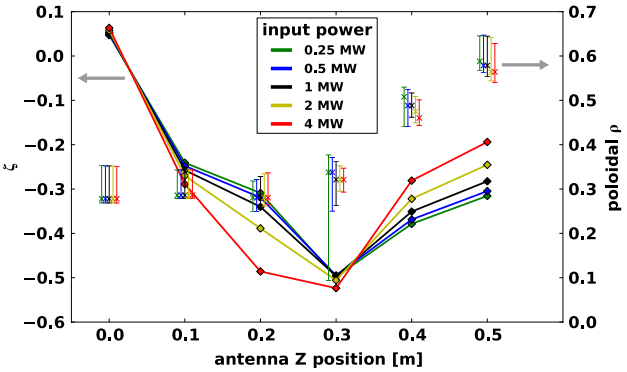

Figure 18. Input power scan of current drive efficiency and radial location of the current peak for 17 GHz NSTX L-mode cases with positive initial $N_\parallel$. Line plots with symbols represent ζ while symbols with vertical error bars represent the radial current location $\rho_{j\,\max}$ and its width σ_j (upper and lower limits represent $\rho_{j\pm1}$). Each group of the cross symbols belongs to one antenna position, and a horizontal shift is employed to separate the lines visually.

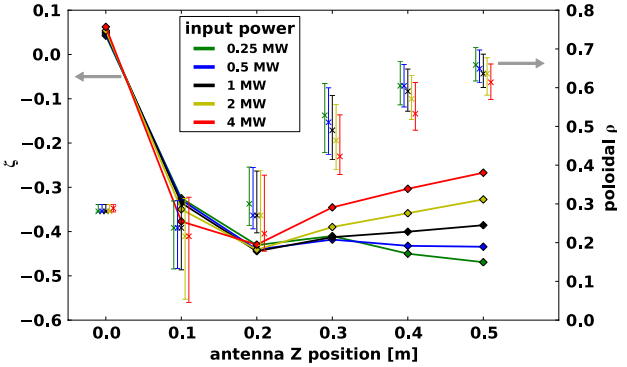

Figure 19. Same as figure 18, but for negative initial $N_\parallel$.

However, in the 0.3 m vertical launch position case (figures 16 and 17), both the power deposition profile and the current drive profile are much broader. This is due to the strongly Doppler-shifted absorption with a relatively large $N_\parallel$ spectral width, as well as Doppler broadening effects [34]. The current is driven in one direction as the sign of $N_\parallel$ is identical for all rays. For this case there is power deposition on overlapping EC harmonics. Moreover, this is one of the interesting cases mentioned in the previous section, in which the Fisch–Boozer current from the deposition on the lower harmonic and the Ohkawa current from the deposition on the higher harmonic are in the same direction.

In this configuration, the power is deposited on suprathermal electrons [34] and EBW H&CD is therefore strongly affected by quasilinear effects. Quasilinear flattening of the distribution function with increasing power levels yields a relative reduction of the absorbed power, resulting in a more inward deposition.

An input power scan for several NSTX L-mode cases is presented in figures 18 and 19. We find that there is no general tendency of the current drive efficiency to increase or decrease with the input power. Cases exist with increasing, decreasing or invariant ζ dependence on input power. However, in most cases, increasing power leads to either lower or similar current drive efficiency. In figures 18 and 19 we also show the current profile maximum radial location ρ_j and its width σ_j, defined as

$$\rho_{j\,\max} \equiv \arg\max_{\rho\in[0,1]} |j(\rho)|\,, \tag{25}$$

$$\rho_{j-1/2} \equiv \min\{\rho : |j(\rho)| = |j(\rho_{j\,\max})/2| \wedge 0 \leqslant \rho < \rho_{j\max}\}, \tag{26}$$

$$\rho_{j+1/2} \equiv \max\{\rho : |j(\rho)| = |j(\rho_{j\,\max})/2| \wedge \rho_{j\max} < \rho \leqslant 1\}, \tag{27}$$

$$\sigma_j \equiv \rho_{j+1/2} - \rho_{j-1/2}. \tag{28}$$

In other words, σ_j corresponds to the full-width at half-maximum if the current profile is considered single-peaked. Increasing power causes the wave absorption to occur further along the direction of propagation, which can either be towards the axis if the absorption occurs on the outboard side or away from the axis in the opposite case. This is caused by the quasilinear flattening of the distribution function and consequently lower absorption rate.

4.3. The effect of $Z_{\rm eff}$

So far we assumed $Z_{\rm eff} = 2$, which is a realistic experimental value. However, $Z_{\rm eff}$ can vary and it is very important to show the effect on EBW performance. We employ here the cases from the previous section and rerun the simulations with $Z_{\rm eff}$ ranging from 1 to 3. Figure 20 shows the effect of $Z_{\rm eff}$ on the current drive efficiency and the position of the current peak. $Z_{\rm eff}$ affects the electron–ion collision frequency and particularly pitch-angle scattering. A larger value of $Z_{\rm eff}$ results in faster isotropization of current-carrying fast electrons. Thus, the current drive efficiency is inversely proportional to $Z_{\rm eff}$ [52]. The general trend of ζ versus $Z_{\rm eff}$ is shown in figure 21. Compared to the $Z_{\rm eff} = 2$ results, the EBW current drive efficiency increases on average by 29% for $Z_{\rm eff} = 1$, while a decrease of 18% is observed for $Z_{\rm eff} = 3$. There is also a minor effect of $Z_{\rm eff}$ on the EBW deposition location, as can be seen in figure 20. This is again caused by the collision frequency change, which affects the plasma quasilinear response to the wave power.

4.4. Robustness

An important factor of any H&CD system is its robustness—the sensitivity to changes in plasma conditions or in the system's parameters. In the previous section we have already investigated what happens if the injected power is changed. Moreover, the effect of changing the vertical launch position can be seen in figures 18 and 19; this effect is rather strong and therefore the vertical launch position must be carefully chosen and controlled. In this section we focus on the EBW H&CD performance sensitivity to plasma parameters.

In figures 22 and 23 we show the sensitivity of EBWs to plasma electron density and temperature variations in the ±50% range. All vertical launch positions and both initial $N_\parallel$ signs of 17 GHz NSTX L-mode cases are used to calculate the medians of absolute location difference $\Delta\rho_{j\,\max}$ and relative current drive efficiency and profile widths $|\Delta\zeta|/|\zeta_0|$ and $|\Delta\sigma_j|/|\sigma_{j0}|$, where the 0 subscripts denote results with the original plasma profiles. We first see a monotonic dependence of all the plotted quantities (except for two cases in $|\Delta\sigma_j|$),

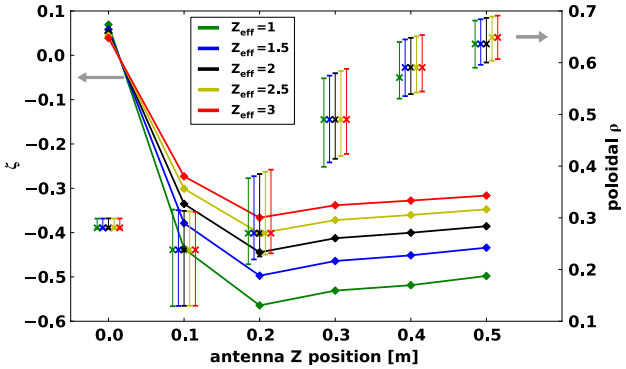

Figure 20. $Z_{\rm eff}$ scan of current drive efficiency and radial location of the current peak for 17 GHz NSTX L-mode cases with negative initial $N_\parallel$, $P_0 = 1$ MW. Line plots with symbols represent ζ while symbols with vertical error bars represent the radial current location $\rho_{j\,\max}$ and its width σ_j (similarly to figure 18).

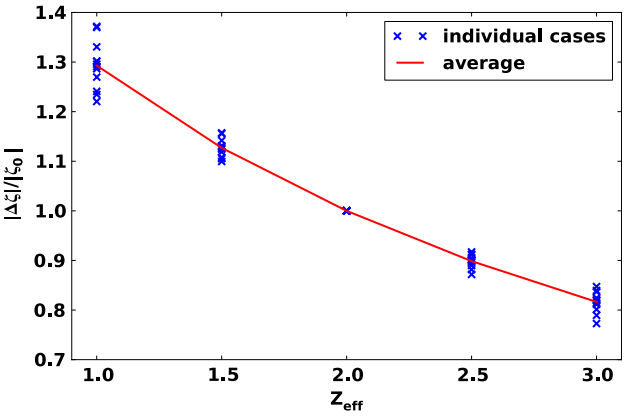

Figure 21. Relative (with respect to $Z_{\rm eff} = 2$ values, denoted as ζ_0) changes of the current drive efficiency versus $Z_{\rm eff}$ for all 17 GHz NSTX L-mode cases with both positive and negative initial $N_\parallel$, $P_0 = 1$ MW.

indicating a non-chaotic behaviour of EBW performance with changing plasma profiles. Quantitatively, the radial current location changes fractionally compared with the typical $\sigma_j \sim 0.1$. However, very precise localization might be important for certain applications, in which case a feedback system is highly advisable. The median difference in current drive efficiency is below 5% for less than 25% changes in the plasma profiles, which is very favourable. The current profile width is slightly more sensitive, a consequence of Doppler broadening. Not shown here are the variances. However, the highest sensitivity is generally observed at lower frequencies, close to a midplane launch where the rays tend to oscillate, leading to current drive efficiencies that are typically low. In most cases the results are close to the median values.

Another parameter that can vary in tokamaks is the plasma current and the toroidal magnetic field. Unlike density and temperature profiles, which are only crudely pre-programmed and evolve during the discharge, it is typical that the plasma current and toroidal magnetic field do not change during the discharge (except, of course, in the start-up and shut-down phases) and that their properties are pre-programmed with high confidence. This makes the demands on the sensitivity on these quantities less stringent as compared with the temperature and

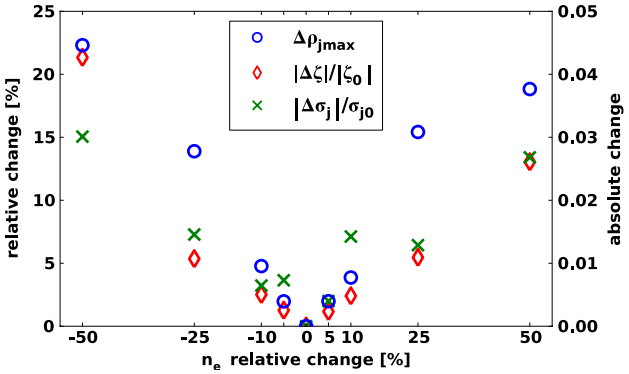

Figure 22. Medians of absolute current location difference $\Delta\rho_{j\,\max}$ and relative current drive efficiency and current profile width differences versus varying plasma electron density. 17 GHz NSTX L-mode 1 MW cases (similarly to figure 18) are used to calculate the medians.

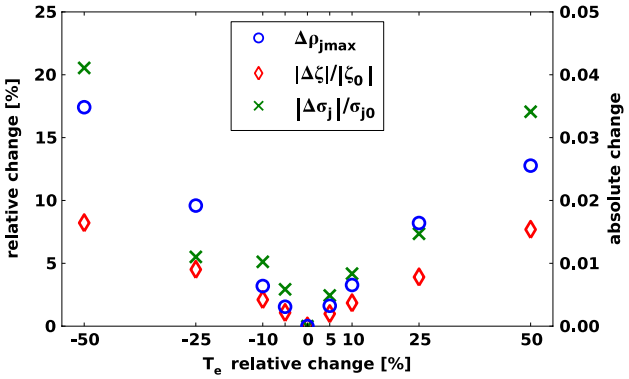

Figure 23. Same as figure 22, but for varying electron temperature.

the density. In figures 24 and 25 we show the sensitivity of 17 GHz L-mode cases to poloidal and toroidal magnetic field changes. The fields are simply changed by multiplying the respective components so that the resulting equilibrium is no longer a solution of the Grad–Shafranov equation. Significantly larger effects of the magnetic field changes on EBW results can immediately be noticed. The sensitivity is particularly high for the toroidal field simply because the toroidal field is much larger than the poloidal field in most of the plasma cross-section. Also notice that changing the total magnetic field by 10% is similar to changing the heating frequency by 1.4 GHz, which is the change in the central $\omega_{\rm ce}$. For large magnetic field changes we can even change the EC absorption harmonic number—e.g. decreasing $B_{\rm tor}$ by 25% shifts 17 GHz into the second harmonic range.

5. Conclusions

By means of coupled ray-tracing and Fokker–Planck simulations, we have thoroughly investigated electron Bernstein wave H&CD prospects for spherical tokamaks. For the first time, a simple analytic formula for the O–X conversion efficiency of a Gaussian beam is derived from 1D plane wave theory. This formula supports our choice of the Rayleigh range as the antenna beam principal parameter that is fixed for all simulated cases. On an extensive set of EBW launch scenarios with varying frequency, vertical antenna position and

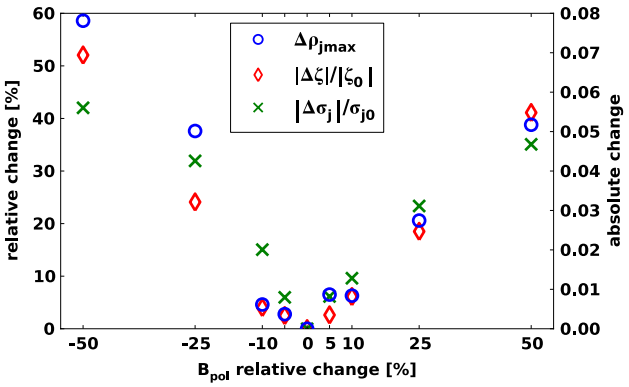

Figure 24. Same as figure 22, but for varying poloidal magnetic field.

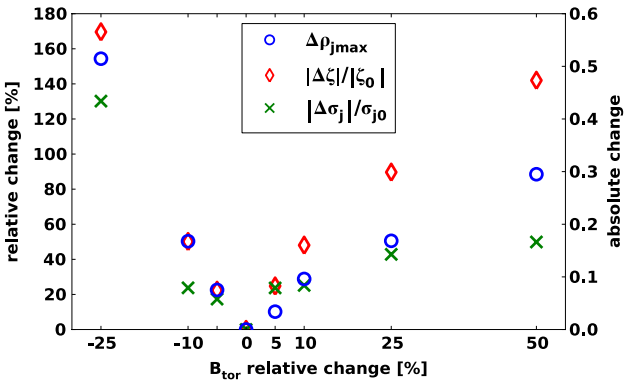

Figure 25. Same as figure 24, but for varying toroidal magnetic field. Results for $B_{tor} - 50\%$ could not be calculated.

toroidal injection angle, we show that EBWs can be absorbed at almost arbitrary radius and that EBWs can drive current with efficiencies comparable to electron cyclotron O- or X-modes. Moreover, the efficiency does not change with radius, while typically the efficiency of X- and O-modes decreases with radius. The best results in terms of efficiency and flexibility are achieved in NSTX plasmas, where the electron cyclotron frequency radial profiles are monotonic. In general, normalized current drive efficiencies $|\zeta|$ on the order of 0.3–0.4 are feasible for all target plasmas, absolute efficiencies then depend on the plasma parameters as $I_{RF}/P_0 \cong 0.31\zeta T_e/R_0 n_e$, where the units are keV for T_e, m for R_0 and 10^{19} m^{-3} for n_e. These results, however, do not reflect the mode-conversion efficiency, which, as we have shown, is limited by the beam divergence and can be further degraded by other effects.

For EBWs, the initial value of $|N_\parallel|$ is fixed by the mode-conversion process and only the sign of $N_\parallel$ can be chosen at will. The evolution of $N_\parallel$ is determined by the wave frequency, the vertical launch position and by the plasma parameters. We have shown how different vertical launch positions strongly influence the $N_\parallel$ spectrum and consequently the current drive efficiency. However, there seems to be no general correlation between the current drive efficiency and the $N_\parallel$ spectrum and its width.

Input power scans have been performed to investigate the quasilinear effects. Increasing power generally leads to either lower or similar current drive efficiency. Higher power also causes the wave absorption to occur further along the direction of propagation, which can either be towards the axis if the absorption occurs on the outboard side or away from the axis in the opposite case. An important factor is the effective ion charge, which affects the electron–ion collisionality, and, consequently, the current drive efficiency significantly depends on Z_{eff}. A minor effect of Z_{eff} on the driven current location can be observed, which is caused by changing the plasma quasilinear response.

The sensitivity of EBW H&CD to changes in plasma parameters has been investigated. It has been shown that the EBW performance is rather robust. Neither the current drive efficiency nor the radial location changes significantly when the electron temperature or density changes moderately. Larger sensitivity is observed for magnetic field changes, especially the (dominant) toroidal field.

In conclusion, the EBW is a promising candidate for a powerful and flexible auxiliary H&CD system for spherical tokamaks, in many aspects comparable to EC systems for standard aspect ratio tokamaks. However, several problems, which are not included in this survey, particularly the coupling, need to be addressed and better understood. High-power experiments on major spherical tokamaks or similar machines would be greatly beneficial to tackle these topics and validate our results.

Acknowledgments

This work was supported by the grant no 202/08/0419 of Czech Science Foundation, the Academy of Sciences of the Czech Republic IRP #AV0Z20430508, the Ministry of Education, Youth and Sports CR #7G10072, US Department of Energy DE-AC02-09CH11466 and European Communities under the contract of Association between EURATOM/IPP.CR No FU07-CT-2007-00060 and under the contract of Association between Euratom and CEA and carried out within the framework of the European Fusion Development Agreement. The views and opinions expressed herein do not necessarily reflect those of the European Commission.

References

[1] Prater R. 2004 *Phys. Plasmas* **11** 2349–76
[2] Peng Y.K.M. *et al* 2005 *Plasma Phys. Control. Fusion* **47** B263–B83
[3] Voss G.M., Davis S., Dnestrovskij A., Kirk A., Knight P.J., Loughlin M., O'Brien M.H., Sychugov D., Tabasso A. and Wilson H.R. 2008 *Fusion Eng. Des.* **83** 1648–53
[4] Kotschenreuther M., Valanju P.M., Mahajan S.M. and Schneider E.A. 2009 *Fusion Eng. Des.* **84** 83–8
[5] Bernstein I.B. 1958 *Phys. Rev.* **109** 10–21
[6] Shevchenko V., Baranov Y., O'Brien M. and Saveliev A. 2002 *Phys. Rev. Lett.* **89** 265005
[7] Laqua H.P., Erckmann V., Hartfuss H.J. and Laqua H. 1997 *Phys. Rev. Lett.* **78** 3467–70
[8] Laqua H.P., Maassberg H., Marushchenko N.B., Volpe F., Weller A. and Kasparek W. 2003 *Phys. Rev. Lett.* **90** 075003
[9] Kessel C.E. *et al* 2006 *Phys. Plasmas* **13** 056108
[10] Preinhaelter J., Laqua H.P., Urban J., Vahala L. and Vahala G. 2009 *Plasma Phys. Control. Fusion* **51** 125008
[11] Urban J., Preinhaelter J., Diem S.J., Laqua H.P., Pavlo P., Shevchenko V., Taylor G., Vahala G., Vahala L. and

Valovic M. 2009 *J. Plasma Fusion Res. Ser.* **8** 1153–7 http://www.jspf.or.jp/JPFRS/PDF/Vol8/jpfrs2009_08-1153.pdf
[12] Decker J. and Peysson Y. 2004 DKE: a fast numerical solver for the 3-D relativistic bounce-averaged electron drift kinetic equation *Report* EUR-CEA-FC-1736 (Cadarache: EURATOM/CEA)
[13] Decker J. 2005 Electron bernstein wave current drive modeling in toroidal plasma confinement *PhD Thesis* (Massachusetts Institute of Technology, Boston, MA)
[14] Urban J., Decker J., Peysson Y., Preinhaelter J., Taylor G., Vahala L. and Vahala G. 2009 *AIP Conf. Proc.* **1187** 465–8
[15] Gates D.A. *et al* 2009 *Nucl. Fusion* **49** 104016
[16] Meyer H. *et al* 2009 *Nucl. Fusion* **49** 104017
[17] Stork D. *et al* 2010 *Proc. 23rd Int. Conf. on Fusion Energy (Daejeon, Korea, 2010)* (Vienna: IAEA) CD-ROM file ICC/P5-06 and http://www-naweb.iaea.org/napc/physics/FEC/FEC2010/html/index.htm
[18] Laqua H.P. 2007 *Plasma Phys. Control. Fusion* **49** R1–42
[19] Ram A.K. and Schultz S.D. 2000 *Phys. Plasmas* **7** 4084–94
[20] Preinhaelter J. and Kopecký V. 1973 *J. Plasma Phys.* **10** 1–12
[21] Preinhaelter J. 1975 *Czech J. Phys.* **25** 39–50
[22] Hansen F.R., Lynov J.P., Maroli C. and Petrillo V. 1988 *J. Plasma Phys.* **39** 319–37
[23] Mjølhus E. 1984 *J. Plasma Phys.* **31** 7–28
[24] Piliya A.D. and Tregubova E.N. 2005 *Plasma Phys. Control. Fusion* **47** 143–54
[25] Urban J. and Preinhaelter J. 2006 *J. Plasma Phys.* **72** 1041–4
[26] Ram A.K., Bers A. and Lashmore-Davies C.N. 2002 *Phys. Plasmas* **9** 409–18
[27] Popov A.Y. 2010 *Plasma Phys. Control. Fusion* **52** 035008
[28] Shalashov A.G. and Gospodchikov E.D. 2008 *Plasma Phys. Control. Fusion* **50** 045005
[29] Irzak M.A. and Popov A.Y. 2008 *Plasma Phys. Control. Fusion* **50** 025003
[30] Köhn A., Cappa Á., Holzhauer E., Castejón F., Fernández Á. and Stroth U. 2008 *Plasma Phys. Control. Fusion* **50** 085018
[31] Gusakov E.Z. and Surkov A.V. 2007 *Plasma Phys. Control. Fusion* **49** 631–9
[32] Xiang N. and Cary J.R. 2008 *Phys. Rev. Lett.* **100** 085002
[33] Goldsmith P.F. 1998 *Quasioptical Systems: Gaussian Beam, Quasioptical Propagation and Applications* (Piscataway, NJ: IEEE)
[34] Decker J. and Ram A.K. 2006 *Phys. Plasmas* **13** 112503
[35] Puri S., Leuterer F. and Tutter M. 1973 *J. Plasma Phys.* **9** 89–100
[36] Saveliev A.N. 2007 *Plasma Phys. Control. Fusion* **49** 1061–74
[37] Piliya A.D., Popov A.Y. and Tregubova E.N. 2005 *Plasma Phys. Control. Fusion* **47** 379–94
[38] Bornatici M., Cano R., Debarbieri O. and Engelmann F. 1983 *Nucl. Fusion* **23** 1153–257
[39] Bernstein I.B. 1975 *Phys. Fluids* **18** 320–4
[40] Ginzburg V.L. and Rukhadze A.A. 1975 *Volny v Magnitoaktivnoi Plazme* (Moscow: Nauka)
[41] Fried B.D. and Conte S.D. 1961 *The Plasma Dispersion Function the Hilbert Transform of the Gaussian* (New York: Academic)
[42] Diem S.J., Taylor G., Caughman J.B., Efthimion P.C., Kugel H., LeBlanc B.P., Phillips C.K., Preinhaelter J., Sabbagh S.A. and Urban J. 2009 *Phys. Rev. Lett.* **103** 015002
[43] Diem S.J. *et al* 2009 *Nucl. Fusion* **49** 095027
[44] Ram A.K., Decker J. and Peysson Y. 2005 *J. Plasma Phys.* **71** 675–93
[45] Nelson-Melby E., Harvey R.W., Smirnov A.P. and Ram A.K. 2007 *Plasma Phys. Control. Fusion* **49** 1913–29
[46] Hawryluk R.J. 1981 *Proc. Int. School of Plasma Physics* vol 1 (Varenna: Pergamon) p 19
[47] Forest C.B., Chattopadhyay P.K., Harvey R.W. and Smirnov A.P. 2000 *Phys. Plasmas* **7** 1352–5
[48] Wagner D.H. *et al* 2009 *IEEE Trans. Plasma Sci.* **37** 395–402
[49] Petty C.C., Prater R., Lohr J., Luce T.C., Fox W.R., Harvey R.W., Kinsey J.E., Lao L.L. and Makowski M.A. 2002 *Nucl. Fusion* **42** 1366–75
[50] Shevchenko V. and Saveliev A. 2009 *AIP Conf. Proc.* **1187** 457–60
[51] Taylor G., Efthimion P.C., Kessel C.E., Harvey R.W., Smirnov A.P., Ershov N.M., Carter M.D. and Forest C.B. 2004 *Phys. Plasmas* **11** 4733–9
[52] Fisch N.J. and Boozer A.H. 1980 *Phys. Rev. Lett.* **45** 720–2
[53] Ohkawa T. 1976 Steady state operation of tokamaks by rf heating *Report* GA-A13847 (San Diego, CA: General Atomics)